Magnetic Resonance Imaging 59 (2019) 137–142

Contents lists available at ScienceDirect

Magnetic Resonance Imaging

journal homepage: www.elsevier.com/locate/mri

Original contribution

Assessing image artifacts from radiotherapy electromagnetic transponders with metal-artifact reduction imaging

Robert V. Bergen[a,b,*], Lawrence Ryner[a,b]

[a] Department of Physics & Astronomy, University of Manitoba, Canada
[b] Medical Physics, CancerCare Manitoba, Canada

ARTICLE INFO

Keywords:
Image artifacts
VAT
SEMAC
Electromagnetic transponder

ABSTRACT

Image artifacts due to 14 gauge radiotherapy electromagnetic (EM) transponders were assessed on conventional spin echo images, and corrected using metal artifact reduction techniques: high bandwidth, view angle tilting (VAT), and slice encoding for metal artifact correction (SEMAC). Large areas of signal loss and/or pile-up were produced in an area extending up to 15.3 mm in radius for 14G transponders in standard imaging. Using high bandwidth imaging with VAT, in-plane artifact sizes were reduced by up to 35%. SEMAC did not significantly reduce in-plane or through plane artifact size for axially oriented images, but was effective in reducing through-plane artifacts for sagittal images. Using the experimental data, magnetic field maps were simulated so that the magnetic susceptibility of the transponder could be estimated and slice profiles could be visualized. Due to the large susceptibilities involved, current correction techniques are unable to fully correct artifacts due to EM transponders and significant areas of signal loss and distortion remain. Care should be taken when planning MRI following EM transponder implantation.

1. Introduction

Recently, electromagnetic (EM) transponders have been developed to provide continuous real-time tracking of organ motion during radiotherapy treatment [1,2]. EM transponders are passive devices consisting of a copper coil wound about a ferromagnetic core, and are implanted in a similar manner to fiducial markers. EM transponders can be electronically tracked in real-time during radiotherapy treatment to assist in tumor localization and to avoid large doses of radiation and associated toxicity to nearby critical organs at risk [3–6]. This is especially important for organs that may move during the course of treatment [7–10].

Conformal radiotherapy techniques like intensity modulated radiotherapy (IMRT) [11] and volumetric modulated arc therapy (VMAT) [12] deliver highly accurate, escalated doses in complex spatial distributions. Magnetic resonance imaging (MRI) can provide excellent anatomical as well as functional information and MR images are often co-registered with CT images for tumor localization and radiotherapy planning [13,14]. However, MRI is prone to magnetic susceptibility artifacts which may limit the usefulness of MR-guidance for patients implanted with ferromagnetic EM transponders [15].

Metal artifact correction techniques in MRI may be used to reduce the size of susceptibility artifacts induced by metal objects in the patient. These sequences may use a combination of high receiver and high radiofrequency (RF) pulse bandwidths, view angle tilting (VAT) and slice encoding for metal artifact correction (SEMAC) to correct metal implant induced artifacts. VAT applies additional gradients during image acquisition which counters inhomogeneous field effects in-plane [16], while SEMAC spatially encodes the image in the slice encoding direction to resolve through-plane distortions [17,18].

This study assesses the artifact sizes for 14 gauge EM transponders with standard T_2-weighted spin echo pulse sequences and quantifies the reduction in artifact size using high receiver/RF bandwidth, VAT, and SEMAC.

2. Methods

Assessment of 14 gauge radiotherapy electromagnetic transponders (Varian Medical Systems, Palo Alto, CA) was performed on a 3 T Siemens Verio MRI scanner. Axial and sagittal T_2 images were acquired at a FOV of 200 × 200 mm, slice thickness of 3 mm, with a bandwidth of 256 Hz/px and TE/TR = 96/5200 ms.

Metal artifact reduction techniques were applied using the WARP pulse sequence (Siemens, Munich, Germany) which acquires high-bandwidth turbo spin echo images with optional settings for VAT, and SEMAC. Axial and sagittal high readout/RF bandwidth images were

* Corresponding author at: 675 McDermot Ave, R3E 0V9 Winnipeg, Manitoba, Canada.
E-mail address: rbergen4@cancercare.mb.ca (R.V. Bergen).

https://doi.org/10.1016/j.mri.2019.02.005
Received 16 November 2018; Received in revised form 31 January 2019; Accepted 14 February 2019

acquired at FOV = 180 × 180 mm, resolution = 0.7 × 0.7 mm, slice thickness 3 mm at 930 Hz/pixel receiver bandwidth and 2 kHz RF pulse bandwidth, both with and without VAT. Images were then acquired with 5, 10 and 15 slice encoding steps with SEMAC.

Phantoms were constructed by placing the electromagnetic transponders in a solution of 1 g/L agar gel, oriented with the long axis either parallel or perpendicular to the main field. The imaging plane was chosen to be either axial or sagittal.

Artifact radius was determined by ASTM standard, where the artifact fringe is defined by signal intensity fluctuations of more than 30% of the mean value when no artifact is present [19]. This radius does not include the radius of the transponder itself. The artifact radius was manually measured on a slice containing the largest artifact, and the number of slices in which an artifact appeared was counted. Error in the measurements was assumed to be +/−1/2 pixel (+/−0.4 mm). Magnetic field simulations were carried out in COMSOL Multiphysics (COMSOL, Stockholm, Sweden). The electromagnetic transponder was modelled as a cylinder with radius 0.9 mm, and length 8.5 mm.

3. Results

3.1. In-plane artifact size

The presence of the EM transponder caused large areas of signal loss and/or pile-up in artifacts extending up to 15.3 mm and 14.4 mm in radius for transponders in standard axial and sagittal spin echo images, respectively (Fig. 1). Results for sagittal images are measured in the read direction where the artifact radius is largest. In axial imaging, high receiver bandwidth and high bandwidth RF pulses reduced the artifact size to 10.5 mm. This corresponded to a 31% reduction in artifact size compared to the spin echo sequence. In addition to high receiver/RF pulse bandwidth, VAT (Fig. 3), and SEMAC (Fig. 4) were also added to the pulse sequence. Artifact size with VAT enabled was found to be 9.8 mm (35% reduction), and artifact size with SEMAC enabled was 10.5 mm (31% reduction). Artifact size for sequences combining VAT and 5, 10 and 15 SEMAC encoding steps was also tested, with artifact size measuring 9.8 mm in each case, showing no change compared to images using only VAT (Fig. 5). In-plane artifact reductions for all axial as well as sagittal images are presented in Table 1.

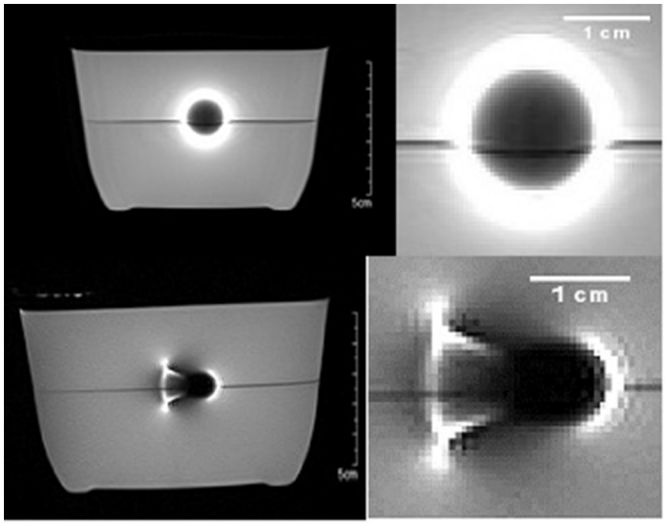

Fig. 1. Top: Conventional spin-echo axial image. A zoomed view of the artifact due to the electromagnetic transponder is on the right. Bottom: Conventional spin-echo sagittal image.

3.2. Through-plane artifact size

The number of slices in which artifacts could be detected was counted for each imaging sequence. All axial images had 12 slices in which artifacts were present, regardless of imaging settings. The sagittal image with high readout/RF bandwidth with VAT and SEMAC enabled had 6 slices with artifacts present. All other sagittal images had 9 slices with artifacts present. These measurements are presented in Table 2.

3.3. Magnetic field simulations

Magnetic field simulations were carried out using the known transponder dimensions and various magnetic susceptibilities until the simulated artifact was approximately the same size as the measured artifact. The estimated magnetic susceptibility of the transponder was $\chi = 10^{-2}$.

Slice profiles of the WARP image were also simulated. The magnetic field inhomogeneity ΔB_0 was plotted in kHz and is shown in Fig. 6. After adding a slice encoding gradient, bands of width 2 kHz may be colour coded to visualize changes in slice thickness due to the presence of the transponder (Fig. 6). A three dimensional visualization of the slice profiles was also generated from the magnetic field simulations. Fig. 7 shows three slices at different distances from the transponder centered at (x,y,z) = (50,50,23). Magnetic field simulations were also performed for a 1.5 T B_0 field for comparison (Fig. 8).

4. Discussion

4.1. Artifacts in axial imaging

Large artifacts were observed in spin echo imaging for EM transponders due to their ferromagnetic cores, which have a magnetic susceptibility many orders of magnitude higher than that of tissue or water. ($X_{ferro} \gg X_{tissue} \approx X_{water} \approx -9 \times 10^{-6}$). From our magnetic field simulations, the inhomogeneity lies well outside the 30 kHz range, reaching magnitudes of over 200 kHz near the transponder. Therefore, in this region, spins will not be excited by the initial RF pulse since they precess at frequencies well outside the range of the RF bandwidth. This explains the central areas of signal loss seen in Figs. 1–5.

Another characteristic of the artifacts in Figs. 1–5 is a bright ring of signal distortion which surrounds the central area of signal loss. This can be explained by large through-plane distortions, and can be better understood through an examination of the slice profiles near the EM transponder. Fig. 6 shows the slice profiles near the EM transponder, when the transponder axis was oriented parallel to the B_0 field. As a slice select RF pulse is played out, spins within a 2 kHz bandwidth are excited. However, as Fig. 6 shows, the inhomogeneity due to the EM transponder greatly affects the spatial encoding of the slice select gradient. Many of the slice select pulses excite a heavily distorted slab, as well as a thin shell several millimeters away. For example, the RF pulse that excites the spins in the yellow slice at z = 30 mm will also excite a region at z = 18–20 mm. This results in signal pile up, as all these spins are erroneously encoded at z = 30 mm. Nearer to the transponder, slice thickness rapidly shrinks resulting in signal loss.

Beyond the massive signal pile-up and signal void artifacts shown in Figs. 1–5, there is also a surrounding area in which smaller signal intensity changes occur. The boundary where signal intensity fluctuations exceed 30% is not obvious from the images shown, and therefore the artifacts in Figs. 1–5 may appear slightly smaller than reported.

Fig. 7 shows 3D representations of three slice profiles (z = 12, 18 and 30 mm). The slice profiles are cross-sectioned at x = 50 mm to better visualize slice thickness. The bottom right panel shows the full slice at z = 30 mm. Far from the artifact, little distortion of the slice is seen, and a very thin region of space above the slice is also excited. The bright ring artifacts seen in Figs. 2–4 are a result of the projection of these spins onto the slice. As the imaging slice approaches the

Table 1
In-plane artifact radii (mm) for all imaging sequences with axial and sagittal orientations. The artifact radii presented here are from the imaging slice where the artifact was largest. The last column refers to a SEMAC sequence with 15 slice encoding steps. Percent reductions of the artifact are listed in brackets.

	Conventional spin echo	High readout/RF bandwidth	High readout/RF bandwidth + VAT	High readout/RF bandwidth + VAT + SEMAC
Axial	15.3	10.5 (31%)	9.8 (35%)	10.5 (31%)
Sagittal	14.4	9.8 (32%)	9.8 (32%)	10.5 (27%)

Table 2
Through-plane artifact sizes for all imaging sequences with axial and sagittal orientations. The measurements presented here are the number of slices in which artifacts were detected. The last column refers to a SEMAC sequence with 15 slice encoding steps. Percent reductions of the artifact are listed in brackets.

	Conventional spin echo	High readout/RF bandwidth	High readout/RF bandwidth + VAT	High readout/RF bandwidth + VAT + SEMAC
Axial	12	12 (0%)	12 (0%)	12 (0%)
Sagittal	9	9 (0%)	9 (0%)	6 (33%)

transponder, this region becomes thicker, and the ring artifact becomes brighter.

4.1.1. Artifact reductions – axial imaging

Advanced metal artifact reduction sequences which use high receiver/RF pulse bandwidth reduced the artifact size by 31%. The additional use of VAT marginally reduced the artifact size further under an axial orientation to 35%. Applying SEMAC techniques separately or in combination with VAT did not reduce the artifact size any further. Interestingly, there was a marginal increase in in-plane artifact size when SEMAC was applied (Table 1). SEMAC did not appear to be useful when imaging in an axial orientation since the number of slices in which artifacts could be detected did not decrease (Table 2). These observations can be explained by an examination of the magnetic field inhomogeneity due to the transponder shown in Fig. 8. Along the z-direction, the inhomogeneity sharply rises from approximately 4 kHz to 15 kHz across a span of only a few millimeters. Thus, the magnitude of the magnetic field inhomogeneity as well as its gradient is simply too large for SEMAC to resolve. In the y-direction, the gradient of the field inhomogeneity is less steep and has a smaller magnitude, and therefore may be more easily corrected. This will be an important consideration when moving to a sagittal imaging orientation.

4.2. Artifacts in sagittal imaging

Sagittal in-plane artifact radii for all sequences were either marginally smaller or the same size as their axial counterparts (Table 1.) These radii are measured along the z-direction, which is the direction in which the gradient of the field inhomogeneity is the largest (Fig. 8). Large signal intensity distortions are also seen here due to the large through-plane distortions discussed in Section 4.1. However, the magnitude of the field inhomogeneity is slightly reduced along the through-plane direction in this orientation. As a result, fewer slices have detectable artifacts in sagittal imaging compared to axial (Table 2).

4.2.1. Artifact reductions – sagittal imaging

Due to the new orientation, the smaller gradients in the field inhomogeneity now lie in the through-plane direction (y-direction in Fig. 8) and the larger gradients lie in-plane. Due to these changes, it is expected that VAT be less effective in reducing in-plane artifacts in the sagittal orientation compared to axial, while SEMAC be more effective in reducing through-plane artifacts in the sagittal orientation compared to axial. This matched our observations, as VAT did not reduce in-plane artifact size (Table 1), and SEMAC reduced the number of slices which had detectable artifacts by 33%.

4.3. Limitations of VAT and SEMAC

VAT is used to counter in-plane inhomogeneities and so was not very effective at reducing the artifacts which our simulations suggest are dominated by through-plane distortions. SEMAC, on the other hand, resolves through-plane distortion through use of an additional z-phase encoding gradient but complications arise when through-plane inhomogeneities are larger than the z-phase gradient and the excitation profile is not correctly resolved [18]. For SEMAC to fully resolve through-plane distortions, the number of slice encodes should be at least $+/-\left(\frac{\Delta B_0}{BW_{RF}}\right)$ [18]. Our simulations that suggest that the number of slice encodes should be on the order of 300 to fully resolve through-plane distortions due to the EM transponder. However, the acquisition time of this sequence would become excessive. Our sequences were acquired in 44 s without SEMAC, and in 3:08 min with five slice encodes. Each five additional slice encodes added another 3 min to our acquisitions. A fully resolved image of the transponder would therefore require well over an hour of scan time.

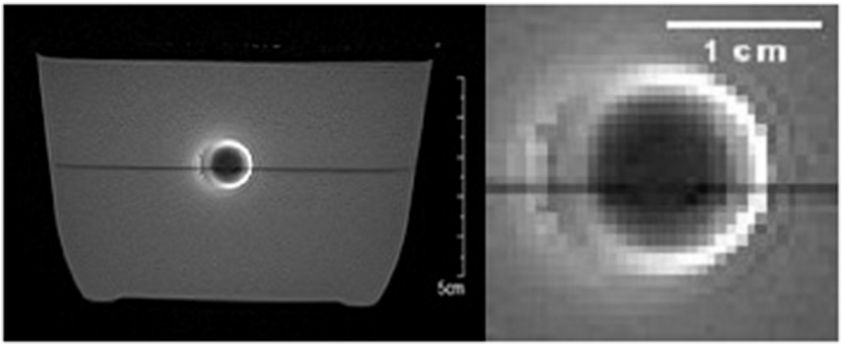

Fig. 2. Left: Axial WARP image with high readout and RF bandwidth.
Right: Artifact due to electromagnetic transponder (zoomed).

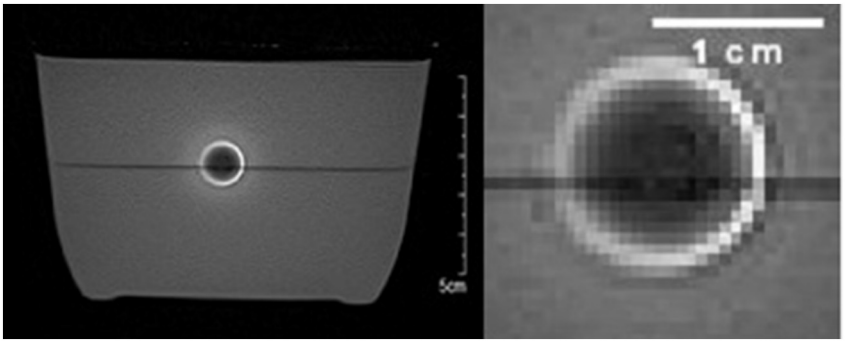

Fig. 3. Left: Axial WARP image with VAT enabled.
Right: Artifact due to electromagnetic transponder (zoomed).

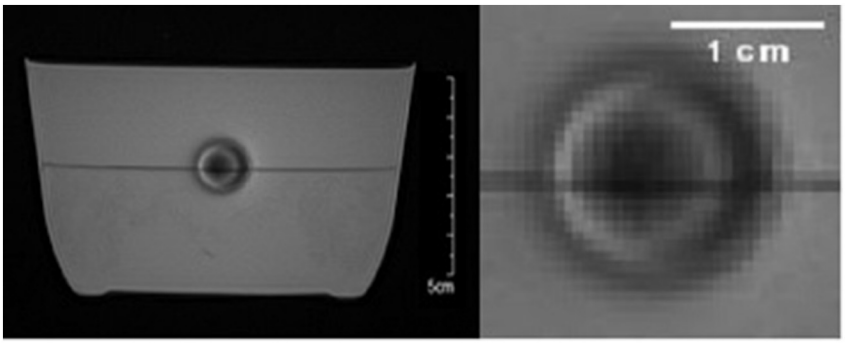

Fig. 4. Left: Axial WARP image with SEMAC enabled.
Right: Artifact due to electromagnetic transponder (zoomed).

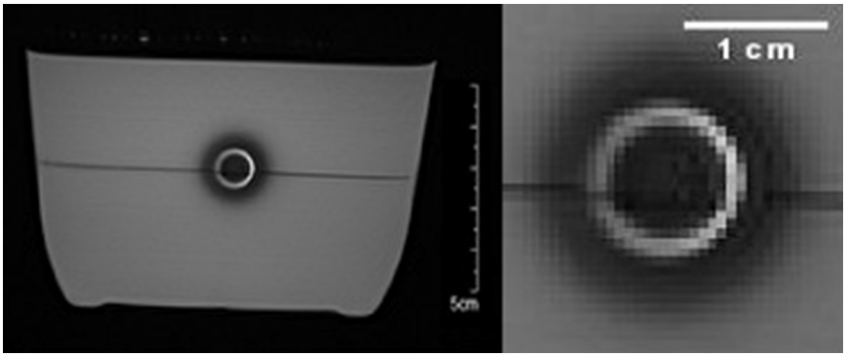

Fig. 5. Left: Axial WARP image with VAT and SEMAC enabled.
Right: Artifact due to electromagnetic transponder (zoomed).

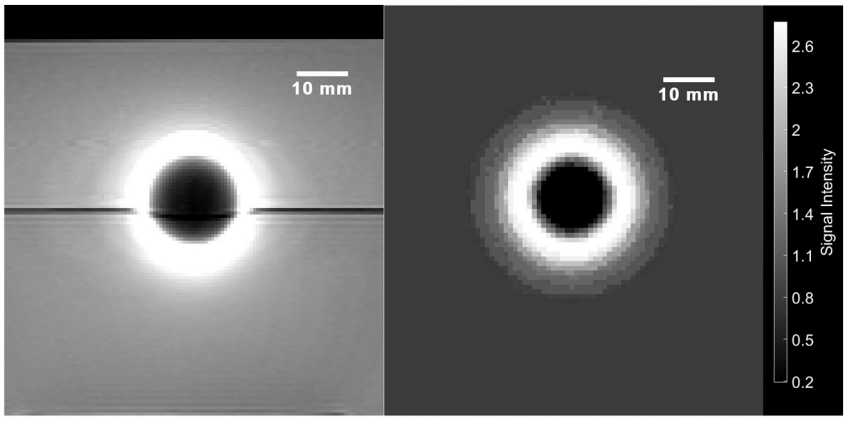

Fig. 6. Left: Magnetic field inhomogeneity (kHz) in the y-z plane due to the EM transponder centered at (x,y,z) = (50, 50, 23). Right: A slice encoding gradient is added to the field map to generate slice profiles of bandwidth 2 kHz for an axial image (width of 3 mm). The EM transponder is oriented with its axis parallel to the main field. Due to large field fluctuations, slice profiles are significantly warped. Thinner slices result in signal loss while thicker slices result in signal pile-up. Close to the transponder, huge changes in the slice profile are observed.

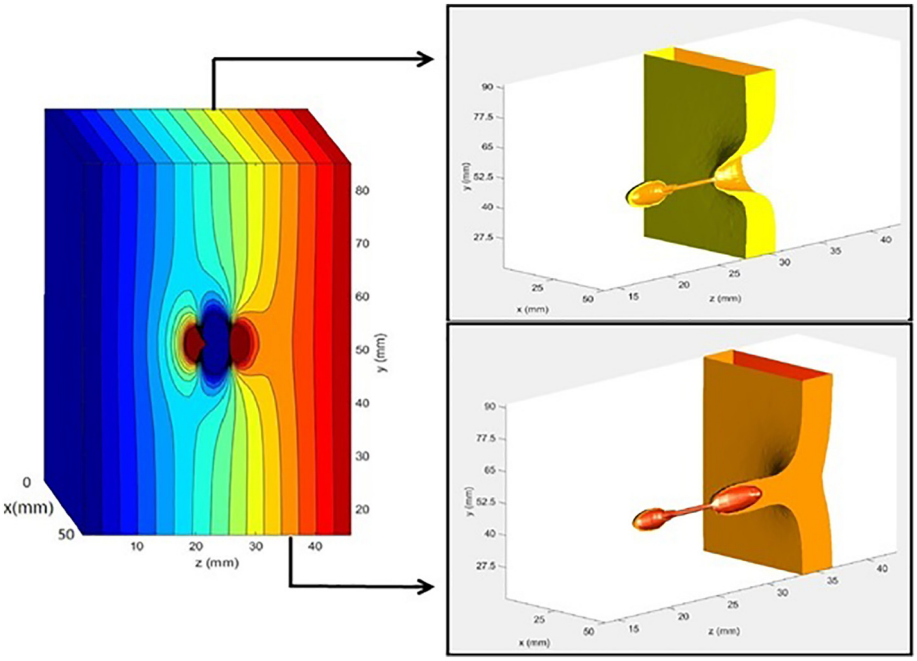

Fig. 7. 3-Dimensional representations of the slice profiles shown in Fig. 7. Slices at z = 12, 18, 30 are shown. The first three slice profiles are cross-sectioned at x = 50 mm to better visualize changes in slice thickness near the transponder. The full slice profile at z = 30 is shown in the bottom right.

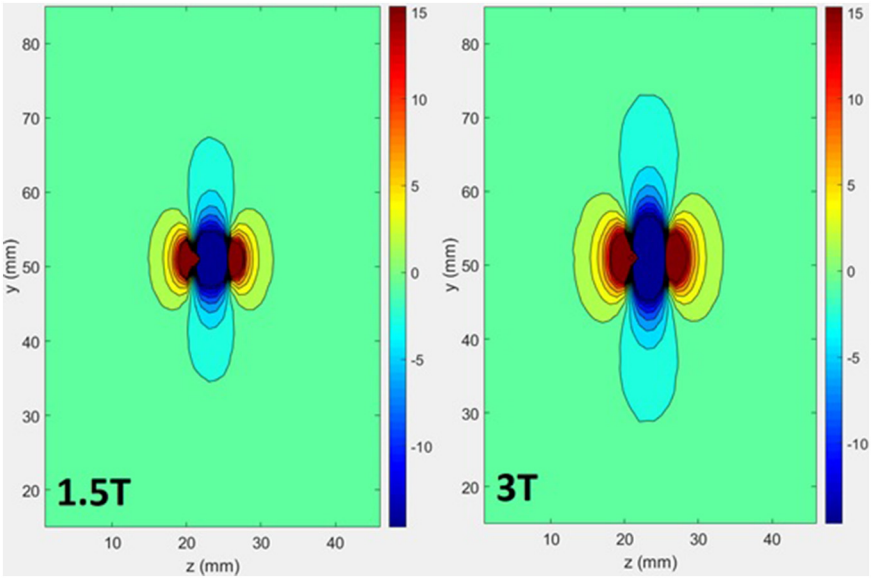

Fig. 8. Magnetic field inhomogeneity (kHz) due to an EM transponder in a 1.5 T (left) and 3 T (right) external field. Isocontours recede several millimeters in the y-direction, but only marginally in the z-direction. Maximum field inhomogeneities are reduced by half under the 1.5 T external field, but are still on the order of several hundred kHz.

4.4. Artifacts at 1.5 T

Phantom data at 1.5 T was not acquired, but through magnetic field simulations at 1.5 T, insight on the efficacy of metal artifact reduction techniques using 1.5 T scanners may be gained. Fig. 8 shows the magnetic field inhomogeneity due to a transponder under a 1.5 T external field (left) and a 3 T external field (right). Under a 1.5 T external field, the 1.2 kHz isocontour recedes only by 1.8 mm in the z-direction, while the −0.7 kHz and −2.8 kHz isocontours recede by 6 and 3 mm, respectively, in the y-direction. Maximum field inhomogeneities near the transponder are reduced by half.

This suggests that under an axial orientation, in-plane artifact sizes would likely decrease on the order of several millimeters for both conventional spin echo sequences and high bandwidth sequences. It is possible in this case that VAT would also be more effective at reducing artifact size. However, SEMAC would perform the same or only marginally better than on a 3 T scanner when using between 5 and 15 SEMAC steps. Although half the number of SEMAC steps would need to be added to fully resolve the artifact at 1.5 T, the acquisition time would likely still be over an hour.

In a sagittal orientation at 1.5 T, we predict that in-plane artifacts in the z-direction will be as large, or only marginally smaller than at 3 T. However, artifact size in the other dimensions will likely be reduced on the order of several millimeters. Since field inhomogeneity gradients in the through-plane direction here are smaller, SEMAC will likely be significantly more effective than at 3 T.

4.5. Other factors

Higher receiver bandwidths were also investigated (up to 1149 Hz/px) but it was found that the additional artifact reductions were negligible in both axial and sagittal imaging (results not shown). Orienting

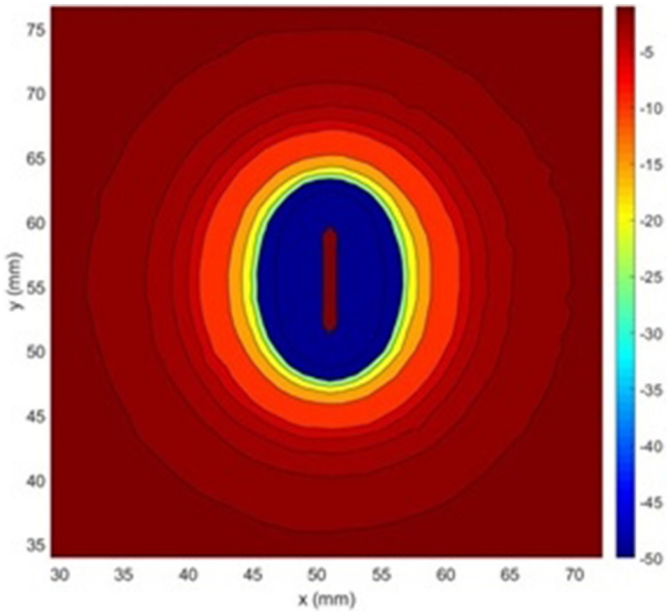

Fig. 9. Magnetic field inhomogeneity (kHz) in the x-y plane with the EM transponder axis perpendicular to the main field. Near the transponder, the inhomogeneity is elliptical as expected. Further away, the field inhomogeneities begin to take on a circular shape and the transponder can be approximated as a point source.

the transponders parallel to the magnetic field versus perpendicular to the field also produced no significant changes in artifact size. These results may initially seem surprising. One might not expect an azimuthally symmetric artifact in an axial image about a cylinder aligned perpendicular to the main magnetic field. Indeed, simulations of the magnetic field with the transponder axis aligned perpendicular to the main field shows elliptical inhomogeneities very near the transponder (Fig. 9). Further away however, the inhomogeneity gradually approaches a circular shape. This suggests transponder orientation only becomes a significant factor with only much larger RF bandwidths (or many more slice encoding steps), which are not feasible at this time.

4.6. Study limitations

One limitation of this study is that we did not investigate the effect of slice thickness for SEMAC scans. Slice thickness was kept constant at 3 mm, but thinner slices require stronger slice encoding gradients which may help reduce artifact size when using SEMAC [18]. However, this would require more slices to cover the same FOV, and SAR may become an issue at 3 T. The additional scan time and loss of SNR are also factors to consider. Additionally, it was challenging to align the miniscule transponder immersed in gel perfectly parallel to or perpendicular to the B_0 field. Some alignment errors of up to approximately ± 5 degrees may have been present during these measurements.

5. Conclusion

Significant image artifacts measuring up to (15.3 +/− 0.4) mm in radius arise in conventional spin echo imaging due to the ferromagnetic core of the electromagnetic transponders. Maximum artifact size and artifact reductions using high receiver/RF pulse bandwidths, VAT, and SEMAC are dependent on image orientation, with maximum reductions of in-plane artifact size of 35% being achieved, and maximum reductions of through plane artifact size of 33% being achieved. We recommend a sagittal orientation for imaging of EM transponders, since through-plane artifacts could not be significantly reduced in the axial orientation. However, in either orientation, significant artifacts remain after metal artifact corrections, which limit the use of MRI close to the transponder. Magnetic field simulations suggest that RF bandwidths approaching hundreds of kHz would be necessary to fully resolve the distortions due to the ferromagnetic EM transponder, which is not feasible with current metal artifact correction techniques.

Acknowledgements

The authors thank Jerry Moran, Siemens Canada Research Collaborations Manager, and Mathias Nittke, Siemens AG, for providing the WARP pulse sequence for evaluation. The authors also thank Varian Medical Systems for providing sample EM transponders.

Funding

This research was funded by the University of Manitoba.

References

[1] Franz AM, Schmitt D, Seitel A, et al. Standardized accuracy assessment of the calypso wireless transponder tracking system. Phys Med Biol 2014;59(22):6797.
[2] Willoughby TR, Kupelian PA, Pouliot J, et al. Target localization and real-time tracking using the Calypso 4D localization system in patients with localized prostate cancer. Int J Radiat Oncol Biol Phys 2006;65(2):528–34.
[3] Booth JT, Caillet V, Hardcastle N, et al. The first patient treatment of electromagnetic-guided real time adaptive radiotherapy using MLC tracking for lung SABR. Radiother Oncol 2016;121(1):19–25.
[4] Schmitt D, Nill S, Roeder F, Gompelmann D, Herth F, Oelfke U. Motion monitoring during a course of lung radiotherapy with anchored electromagnetic transponders: quantification of inter- and intrafraction motion and variability of relative transponder positions. Strahlenther Onkol 2017;193(10):840–7.
[5] Hamilton DG, McKenzie DP, Perkins AE. Comparison between electromagnetic transponders and radiographic imaging for prostate localization: a pelvic phantom study with rotations and translations. J Appl Clin Med Phys 2017;18(5):43–53.
[6] Zhu M, Bharat S, Michalski JM, Gay HA, Hou WH, Parikh PJ. Adaptive radiation therapy for postprostatectomy patients using real-time electromagnetic target motion tracking during external beam radiation therapy. Int J Radiat Oncol Biol Phys 2013;85(4):1038–44.
[7] Crook JM, Raymond Y, Salhani D, Yang H, Esche B. Prostate motion during standard radiotherapy as assessed by fiducial markers. Radiother Oncol 1995;37(1):35–42.
[8] Wu J, Haycocks T, Alasti H, et al. Positioning errors and prostate motion during conformal prostate radiotherapy using on-line isocentre set-up verification and implanted prostate markers. Radiother Oncol 2001;61(2):127–33.
[9] Shirato H, Onimaru R, Ishikawa M, et al. Real-time 4-D radiotherapy for lung cancer. Cancer Sci 2012;103(1):1–6.
[10] Imura M, Yamazaki K, Shirato H, et al. Insertion and fixation of fiducial markers for setup and tracking of lung tumors in radiotherapy. Int J Radiat Oncol Biol Phys 2005;63(5):1442–7.
[11] Intensity Modulated Radiation Therapy Collaborative Working Group. Intensity-modulated radiotherapy: current status and issues of interest. Int J Radiat Oncol Biol Phys 2001;51(4):880–914.
[12] Otto K. Volumetric modulated arc therapy: IMRT in a single gantry arc. Med Phys 2008;35(1):310–7.
[13] McPartlin AJ, Li XA, Kershaw LE, et al. MRI-guided prostate adaptive radiotherapy–a systematic review. Radiother Oncol 2016;119(3):371–80.
[14] Khoo VS, Joon DL. New developments in MRI for target volume delineation in radiotherapy. Br J Radiol 2014;79:S2–15.
[15] Wikstrom J, Isacsson U, Johansson B, Lennernäs BO. Magnetic resonance compatibility of a transponder aimed for radiotherapy positioning – a phantom study. Anticancer Res 2017;37(9):4993–6.
[16] Cho ZH, Kim DJ, Kim YK. Total inhomogeneity correction including chemical shifts and susceptibility by view angle tilting. Med Phys 1988;15(1):7–11.
[17] Kolind SH, MacKay AL, Munk PL, Xiang QS. Quantitative evaluation of metal artifact reduction techniques. J Magn Reson Imaging 2004;20(3):487–95.
[18] Lu W, Pauly KB, Gold GE, Pauly JM, Hargreaves BA. SEMAC: slice encoding for metal artifact correction in MRI. Magn Reson Med 2009;62(1):66–76.
[19] Standard ASTM. F2119–07. Standard test method for evaluation of MR image artifacts from passive implants. West Conshohocken, PA, USA: ASTM International; 2006.